



## Evaluating Gaofen-5 02 EMI-II for atmospheric SO<sub>2</sub> observations: from natural volcanic events to anthropogenic pollution hotspots

Keke Zhu, Jian Chen, Yihui Huang & Hua Cheng


**To cite this article:** Keke Zhu, Jian Chen, Yihui Huang & Hua Cheng (2025) Evaluating Gaofen-5 02 EMI-II for atmospheric SO<sub>2</sub> observations: from natural volcanic events to anthropogenic pollution hotspots, International Journal of Remote Sensing, 46:22, 8820-8833, DOI: [10.1080/01431161.2025.2573241](https://doi.org/10.1080/01431161.2025.2573241)

**To link to this article:** <https://doi.org/10.1080/01431161.2025.2573241>



Published online: 15 Oct 2025.



Submit your article to this journal 



Article views: 39



View related articles 



View Crossmark data 



# Evaluating Gaofen-5 02 EMI-II for atmospheric SO<sub>2</sub> observations: from natural volcanic events to anthropogenic pollution hotspots

Keke Zhu , Jian Chen, Yihui Huang  and Hua Cheng

School of Remote Sensing & Geomatics Engineering, Nanjing University of Information Science & Technology, Nanjing, China

## ABSTRACT

This study presents a comprehensive evaluation of the Gaofen-5 02 Environmental trace gases Monitoring Instrument-II (EMI-II) for retrieving sulphur dioxide (SO<sub>2</sub>) vertical column density (VCD), leveraging comparisons with the TROPospheric Monitoring Instrument (TROPOMI) and Ozone Mapping and Profiler Suite (OMPS). The analysis focuses on the performance of EMI-II in monitoring both natural volcanic emissions and anthropogenic pollution sources. During the 2022 Tonga volcanic eruption, EMI-II effectively detected the westward dispersion of SO<sub>2</sub> plumes, demonstrating strong consistency with TROPOMI observations. For anthropogenic emissions, EMI-II demonstrated robust agreement with TROPOMI and OMPS in mapping SO<sub>2</sub> spatial patterns over the coal-fired power plant cluster in eastern India (17°–25°N, 76°–88°E), achieving spatial correlation coefficients of 0.71 (TROPOMI) and 0.62 (OMPS). However, EMI-II encountered limitations in high-latitude regions of China, where retrieval accuracy was affected by a low signal-to-noise ratio (SNR), large solar zenith angle (SZA), and strong ozone absorption, hindering the detection of weak SO<sub>2</sub> signals. A Sensitivity analysis, conducted using the SCIATRAN radiative transfer model, quantified the influence of total ozone column (TOC), SZA, viewing zenith angle (VZA), and surface albedo on radiance and their impact on SO<sub>2</sub> retrieval. Additionally, the root mean square (RMS) values of spectral fitting residuals in the range of  $1 \times 10^{-3}$  and  $4 \times 10^{-3}$  corresponded to an estimated SO<sub>2</sub> slant column density (SCD) detection limit of approximately 0.15–0.5 Dobson Units (DU). The work provides critical insights into the capabilities and limitations of EMI-II for atmospheric SO<sub>2</sub> monitoring, underscoring its utility in tracking volcanic events and assessing anthropogenic pollution hotspots while identifying key challenges.

## ARTICLE HISTORY

Received 14 May 2025  
Accepted 6 October 2025

## KEYWORDS

Anthropogenic emissions; Environment Monitoring Instrument-II; GaoFen-5; Sulphur dioxide; Vertical column density; Volcanic emissions

## 1. Introduction

Sulphur dioxide (SO<sub>2</sub>) is a critical atmospheric contaminant that considerably affects air quality, climate, and public health. Satellite remote sensing has become an essential tool for monitoring SO<sub>2</sub> emissions on a global scale, providing continuous observations that complement ground-based measurements. A variety of space-borne instruments,

including the Global Ozone Monitoring Experiment (GOME) (Kajino et al. 2011), SCanning Imaging Absorption spectroMeter for Atmospheric CHartographY (SCIAMACHY) (Lee et al. 2008), Ozone Monitoring Instrument (OMI) (McCormick et al. 2015), Global Ozone Monitoring Experiment-2 (GOME-2) (Nowlan et al. 2011), Ozone Mapping and Profiler Suite (OMPS) (K. Yang et al. 2013), and TROPOspheric Monitoring Instrument (TROPOMI) (V. Fioletov et al. 2020), demonstrate exceptional sensitivity in detecting atmospheric SO<sub>2</sub> concentrations and enable continuous spatial monitoring.

The Gaofen-5 O<sub>2</sub> satellite, equipped with the Environmental trace gases Monitoring Instrument-II (EMI-II) (Xia et al. 2024), represents a novel effort in China's satellite-based atmospheric observation. EMI-II, operating in the ultraviolet-visible spectral range, offers potential advantages such as high spectral resolution and wide spatial coverage. In contrast to widely utilized instruments such as TROPOMI and OMPS, the EMI-II instrument faces challenges such as reduced signal-to-noise ratio (SNR) and calibration uncertainties, which affect its SO<sub>2</sub> retrieval accuracy.

Despite recent progress in satellite-based SO<sub>2</sub> retrieval, accurately detecting SO<sub>2</sub> in regions with low-to-moderate emission intensities remains a challenge (V. E. Fioletov et al. 2016; Theys et al. 2015, 2021). The weak contribution of near-surface SO<sub>2</sub> from anthropogenic sources complicates retrievals. In China, stringent emission control policies in recent years have successfully reduced SO<sub>2</sub> levels (Kong et al. 2024; Niu et al. 2023), but this has introduced new uncertainties for EMI-II due to low SO<sub>2</sub> concentrations and weakened SNR under low-pollution conditions. Additionally, complex atmospheric backgrounds further hinder accurate retrievals. Most current SO<sub>2</sub> retrieval methods are optimized for regions with high emissions, such as volcanic eruptions and industrialized hotspots (Krotkov et al. 2016; Li et al. 2017; Theys et al. 2019), and applying these methods in regions with weaker emissions introduces additional uncertainties.

This study systematically evaluates the performance of EMI-II in retrieving SO<sub>2</sub> across different emission scenarios, focusing specifically on its limitations in low-emission and high-latitude regions. By comparing EMI-II's retrievals with well-established datasets like TROPOMI and OMPS, we identify critical parameters that affect its accuracy. The findings offer insights into the strengths and weaknesses of EMI-II, providing guidance for improving its reliability in SO<sub>2</sub> monitoring and informing future developments in satellite sensor technology.

## 2. Data and methods

### 2.1. Data used

The EMI-II instrument on the Gaofen-5 O<sub>2</sub> satellite, launched on 7 September 2021, is engineered to observe the distribution and variation of atmospheric trace gases, providing daily global coverage with a nadir spatial resolution of 13 km (along-track) × 24 km (cross-track) and a local overpass time of 10:30. EMI-II operates across four bands: UV1 (234–311 nm), UV2 (306–401 nm), VIS1 (400–552 nm), and VIS2 (544–714 nm). It enables high-resolution atmospheric observations by detecting ultraviolet and visible radiation reflected or scattered from the Earth's atmosphere and surface. This capability facilitates analysing the distribution and

changes of trace gases, including NO<sub>2</sub>, SO<sub>2</sub>, and O<sub>3</sub>. We derived SO<sub>2</sub> retrievals from the UV2 band of EMI-II.

Since the cloud retrieval algorithm for EMI-II is still under development, cloud data (cloud fraction and cloud pressure) were taken from the TROPOMI cloud product. These data, used for cloud screening and air mass factor (AMF) calculation, were obtained from the Copernicus Data Space Browser. Surface albedo was extracted from the 328 nm data of the GOME-2 monthly LER product (Tilstra et al. 2017). Surface elevation data were sourced from the ETOPO global topographic model.

This study evaluated the accuracy of SO<sub>2</sub> retrievals from the EMI-II instrument by comparing its results with SO<sub>2</sub> products from TROPOMI and OMPS as benchmarks. TROPOMI, recognized as the world's most advanced atmospheric monitoring spectrometer, offers the highest spatial resolution (3.5 km × 5.5 km) and a local overpass time of 13:30 while providing global daily coverage of trace gases such as O<sub>3</sub>, NO<sub>2</sub>, SO<sub>2</sub>, HCHO, CO, and CH<sub>4</sub>. OMPS, onboard the Suomi NPP satellite launched on 28 October 2011 with a local overpass time of 13:30, includes three instruments: OMPS-NM, OMPS-NP, and OMPS-LP. OMPS-NM measures backscattered solar radiation in the wavelength range of 300 to 380 nm at a nadir spatial resolution of 50 km × 50 km. Despite its coarser resolution, OMPS's single detector design improves SNR, making it well-suited for SO<sub>2</sub> observations and widely validated in atmospheric studies (Carn et al. 2015; K. Yang et al. 2013).

## 2.2. Methods

The Differential Optical Absorption Spectroscopy (DOAS) method is widely employed in satellite remote sensing for retrieving SO<sub>2</sub> vertical column density (VCD). The retrieval process consists of two main steps: (1) spectral fitting to derive the slant column density (SCD) and (2) calculating the AMF to convert the SCD into VCD.

### 2.2.1. Theory of optical density fitting

The spectral fitting in the DOAS method is performed using optical depth fitting, as described by the following Equation (1):

$$-\ln\left(\frac{I(\lambda - \Delta(\lambda)) - \text{offset}(\lambda)}{I_0(\lambda)}\right) = \sum_i \sigma'_i(\lambda) SCD_i + P(\lambda) \quad (1)$$

In the equation,  $I$  represents the observed radiance spectrum,  $I_0$  represents the observed irradiance spectrum,  $\Delta(\lambda)$  denotes the wavelength shift of the radiance spectrum, and  $\text{offset}(\lambda)$  accounts for intensity correction.  $SCD_i$  and  $\sigma'_i$  represent the slant column density and absorption cross-section of the gas  $i$ , respectively.  $P(\lambda)$  is a low-order polynomial, using a 5th-order polynomial in this study. The parameters employed in the DOAS fitting process are summarized in Table 1.

Wavelength shifts significantly affect retrieval accuracy in the DOAS algorithm, highlighting the importance of precise wavelength calibration. This ensures the correct mapping between CCD pixels and wavelengths by minimizing a cost function that quantifies the difference between the measured solar spectrum and the high-resolution SAO2010 reference spectrum (K. Chance and Kurucz 2010).



Table 1. Fitting parameters for SO<sub>2</sub> retrieval.

Parameters	Parameter settings
Fitting window	312–326 nm
Reference spectrum	the solar irradiance spectrum
Polynomial	5th order
Cross section	SO <sub>2</sub> (298K) (Vandaele, Hermans, and Fally 2009) O <sub>3</sub> (223K, 243K) (Serdychenko et al. 2014) Pseudo O <sub>3</sub> cross-sections ( $\lambda\sigma_{O_3}$ , $\sigma_{O_3}^2$ ) (Puķīte et al. 2010) NO <sub>2</sub> (220K) (Vandaele et al. 1998) BrO (223K) (Fleischmann et al. 2004) HCHO (298K) (Meller and Moortgat 2000) Raman spectrum (K. V. Chance and Spurr 1997)
Offset correction	1st order

In this study, we employed two pseudo cross-sections, namely  $\lambda\sigma_{O_3}$  and  $\sigma_{O_3}^2$  using the O<sub>3</sub> cross-section at 223 K, to better cope with the strong (non-linear) ozone absorption at short wavelengths (Puķīte et al. 2010). The inclusion of these pseudo absorption cross-sections significantly improved the spectral fitting performance, especially in high-latitude regions. The root mean square (RMS) of the fitting residuals generally decreased by 0% to 50%.

When retrieving SO<sub>2</sub> SCD using the DOAS algorithm, noticeable stripe artefacts are observed in the results for each orbit. These stripe patterns in EMI-II SO<sub>2</sub> retrievals are primarily attributed to instrumental effects (T. Yang et al. 2020) and are essentially fixed with respect to the detector columns. To mitigate this issue, a Fourier transform-based filtering method has been applied to correct the stripe effect. Figure 1 illustrates the comparison of data from a single orbit on 26 July 2023 before and after stripe removal, demonstrating a significant reduction in across-track fluctuations, resulting in a more homogeneous background over the Pacific Ocean.

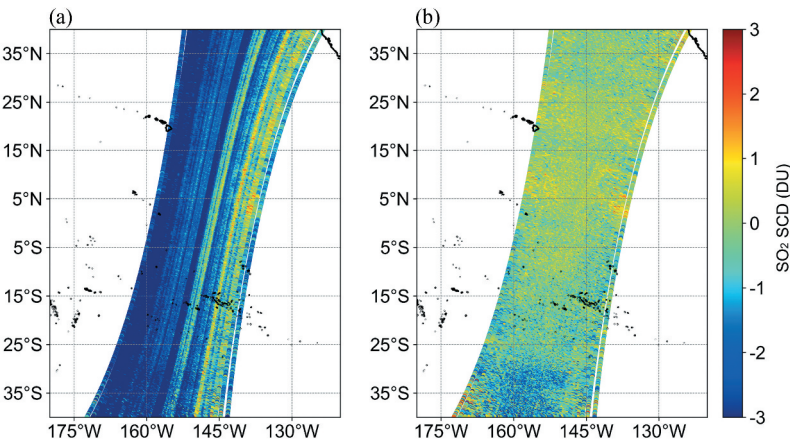


Figure 1. Effect of stripe artefact removal. (a) before stripe removal; (b) after stripe removal.

### 2.2.2. Conversion from SCD to VCD

The SO<sub>2</sub> SCD retrieved using DOAS algorithm represents the total integral of SO<sub>2</sub> density along the photon transmission path. The AMF converts SCD to VCD, independent of the observation geometry. The relationship between the SCD and VCD is given by:

$$VCD = \frac{SCD}{AMF} \quad (2)$$

The AMF calculation is based on the formulation of Palmer et al. (2001):

$$AMF = \int m(p) \cdot s(p) dp \quad (3)$$

Where  $m(p)$  represents the weighting function, also known as the box air mass factor, while  $s$  denotes the normalized a priori SO<sub>2</sub> mixing ratio profile as a function of pressure ( $p$ ). In the AMF computation, the ground and clouds are treated as Lambertian reflectors, and the calculation utilizes pre-computed box air mass factor lookup tables (LUTs) at 313 nm. The SCIATRAN model (Rozanov et al. 2017) is employed to calculate it in this study. Several parameters govern the LUTs, including observation geometry, total ozone column (TOC), surface/cloud pressure, and surface albedo. The observation geometry includes solar zenith angle (SZA), viewing zenith angle (VZA), and relative azimuth angle. The TOC is crucial in accurately retrieving boundary layer SO<sub>2</sub> using the 312–326 nm spectral window.

To calculate the AMF of cloudy pixels, this study employs the independent pixel approximation (Martin 2002) method. In this approach, the inhomogeneous satellite pixel is treated as two independent homogeneous scenes, one completely clear ( $AMF_{\text{clear}}$ ) and the other completely cloudy ( $AMF_{\text{cloud}}$ ). Thus, the cloud-corrected AMF is then expressed as:

$$AMF = \omega AMF_{\text{cloud}} + (1 - \omega) AMF_{\text{clear}} \quad (4)$$

Where  $\omega$  denotes the cloud function.

## 3. Results and discussion

### 3.1. High-emission volcanic SO<sub>2</sub>

The EMI-II instrument demonstrated adequate SNR to detect SO<sub>2</sub> signals in volcanic environments with high SO<sub>2</sub> emissions. A notable case study was the large-scale eruption of the Hunga Tonga-Hunga Ha'apai underwater volcano (20.54°S, 175.38°W) on 14 January 2022, at 04:00 local time. This event released substantial amounts of SO<sub>2</sub> over an extended period, providing an ideal scenario for evaluating EMI-II's performance in monitoring volcanic emissions.

Figure 2(a-d) showed the SO<sub>2</sub> VCD retrieved by EMI-II and TROPOMI on 17 and 18 January 2022, with a spatial resolution of 0.2° × 0.2°. Both instruments successfully captured SO<sub>2</sub> plumes from the eruption, showing a clear westward dispersion driven by easterly winds, consistent with the findings of Xia et al. (2024). The spatial differences in SO<sub>2</sub> distributions between EMI-II and TROPOMI on the same day were attributed to their different overpass times of the two instruments.

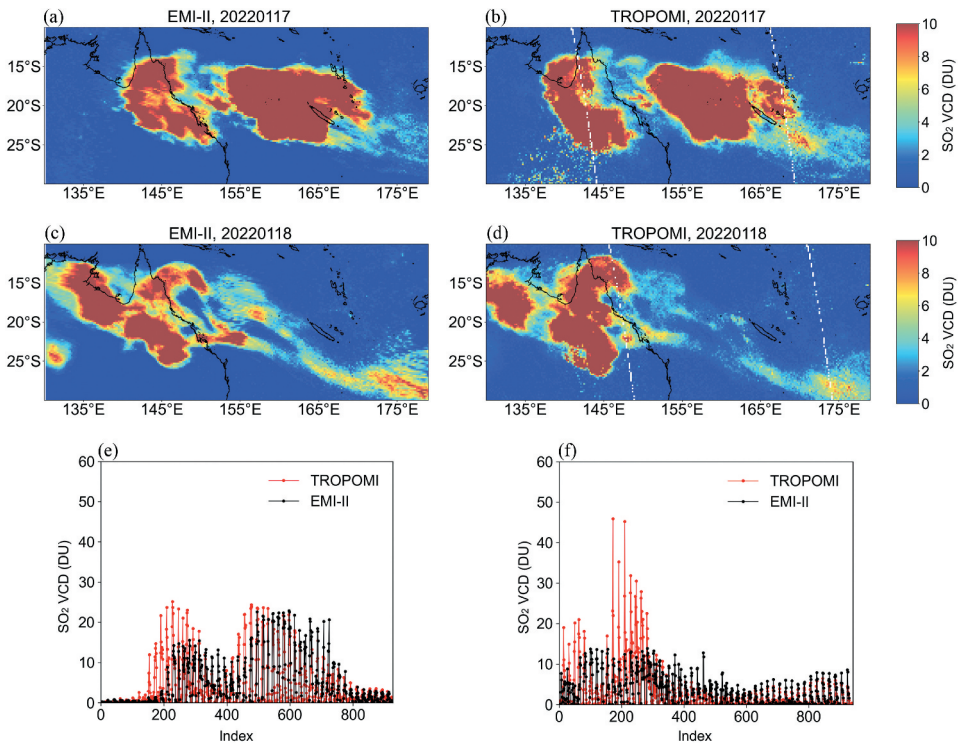


**Figure 2.** SO<sub>2</sub> observations of the Tonga eruption. (a) SO<sub>2</sub> VCD retrieved from EMI-II on 17 January 2022; (b) SO<sub>2</sub> VCD observed by TROPOMI on 17 January 2022; (c) SO<sub>2</sub> VCD retrieved from EMI-II on 18 January 2022; (d) SO<sub>2</sub> VCD observed by TROPOMI on 18 January 2022; (e) comparison of SO<sub>2</sub> VCD between EMI-II and TROPOMI on 17 January 2022; (f) comparison of SO<sub>2</sub> VCD between EMI-II and TROPOMI on 18 January 2022.

To facilitate comparison, the data from EMI-II and TROPOMI were resampled to a  $1^\circ \times 1^\circ$  grid, and pixel-averaged values were analysed. The results (Figure 2(e, f)), evaluated with a 99.5% confidence interval, showed that the SO<sub>2</sub> VCD from the Tonga eruption predominantly ranged between 0 and 20 Dobson Units (DU) over the two-day period in the retrieved region. Notably, EMI-II retrievals in high-concentration regions were systematically lower than those from TROPOMI. This difference is likely related to the use of different a priori SO<sub>2</sub> profiles in the AMF calculation.

### 3.2. Anthropogenic SO<sub>2</sub>: emission hotspots and regional differences

#### 3.2.1. Anthropogenic SO<sub>2</sub> hotspots observations in India

India has become the world's largest anthropogenic SO<sub>2</sub> emitter, surpassing China in recent years due to rapid industrialization and economic growth (Li et al. 2018). Additionally, the relatively low latitude of India (mostly between 8°N and 37°N) results in a small SZA, which reduces atmospheric scattering and absorption interference in the ultraviolet spectrum. This improves the sensitivity of EMI-II to SO<sub>2</sub> absorption features, making India an ideal region for evaluating the performance of the instrument in monitoring anthropogenic emissions.

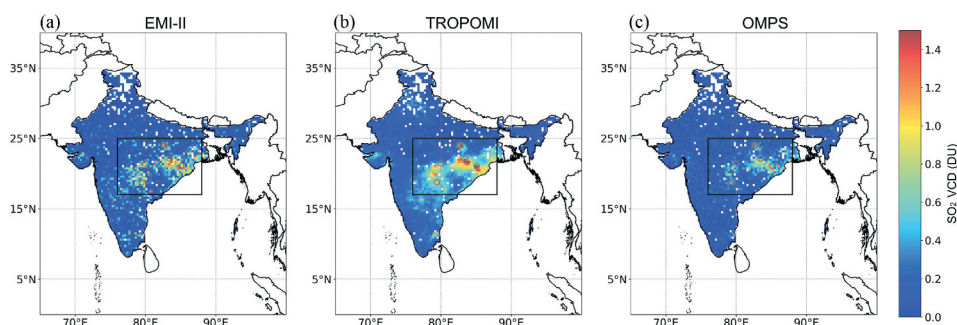


**Figure 3.** Spatial distribution over India. Comparisons of SO<sub>2</sub> column densities retrieved by EMI-II (a), TROPOMI (b), and OMPS (c) over India are presented for relatively clear-sky days from 2022 to 2024, illustrating the spatial distributions derived from the three satellite instruments. EMI-II, TROPOMI, and OMPS effectively capture the heavily polluted regions (rectangular regions), with grey circles indicating the locations of seven coal-fired power plants with capacities greater than 3000 MW.

The results presented the spatial distribution of SO<sub>2</sub> concentrations over India, retrieved by EMI-II for relatively clear-sky days from 2022 to 2024 (Figure 3). TROPOMI and OMPS observations on the same dates were used to evaluate the performance of EMI-II by selecting clear-sky pixels with cloud fractions less than 0.3 and surface albedos less than 0.3. To account for the varying spatial resolutions of the instruments, the study area was divided into 0.3° grid cells, and the average SO<sub>2</sub> VCD within each cell was calculated for comparison. While the three instruments vary in spatial resolution and sensitivity to fine-scale SO<sub>2</sub> variations, they consistently detected a distinct high-concentration pollution belt in eastern India. This region has emerged as a global hotspot for high SO<sub>2</sub> concentrations due to its extensive industrial bases and densely clustered coal-fired power plants (Garg et al. 2001).

EMI-II retrievals of SO<sub>2</sub> VCD exceeding 1.0 DU were primarily concentrated in Odisha, Chhattisgarh, Jharkhand, and West Bengal. The spatial distribution of these high values closely matched the TROPOMI and OMPS results, confirming EMI-II's ability to capture SO<sub>2</sub> signals and identify high-emission regions effectively. Notably, SO<sub>2</sub> VCD exceeded 1.2 DU around major coal-fired power plants such as Vindhyachal, Tamnar, and Talcher Kaniha Super Thermal power stations, further highlighting EMI-II's effectiveness in monitoring strong emission sources.

In heavily polluted areas (17°–25°N, 76°–88°E), the spatial distribution of SO<sub>2</sub> concentrations retrieved from EMI-II showed good agreement with that from TROPOMI, with a spatial correlation coefficient (*R*) of 0.71 and a root mean square error (RMSE) of 0.36 DU. Similarly, EMI-II retrievals also exhibited a reasonable correlation with OMPS data, with a spatial *R* of 0.62 and an RMSE of 0.29 DU, as illustrated in Figure 4. The observed differences were likely attributable to the three-hour temporal offset among EMI-II, TROPOMI, and OMPS, as well as to meteorological variability. This overall consistency across instruments highlighted EMI-II's capability in capturing SO<sub>2</sub> pollution patterns over India, especially in regions characterized by strong anthropogenic emissions.

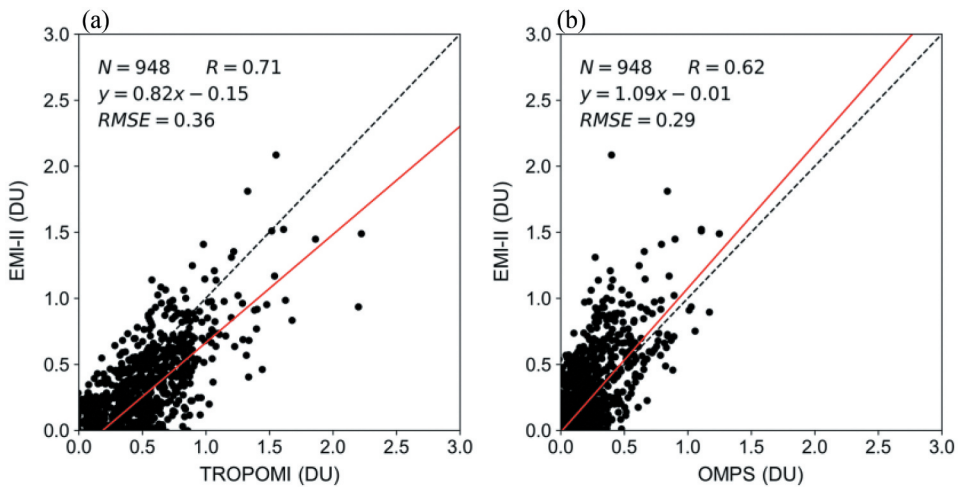


**Figure 4.** Validation of satellite-derived SO<sub>2</sub> column densities over heavily polluted areas. (a) EMI-II vs. TROPOMI; (b) EMI-II vs. OMPS.

### 3.2.2. Low-emission SO<sub>2</sub> observations in China

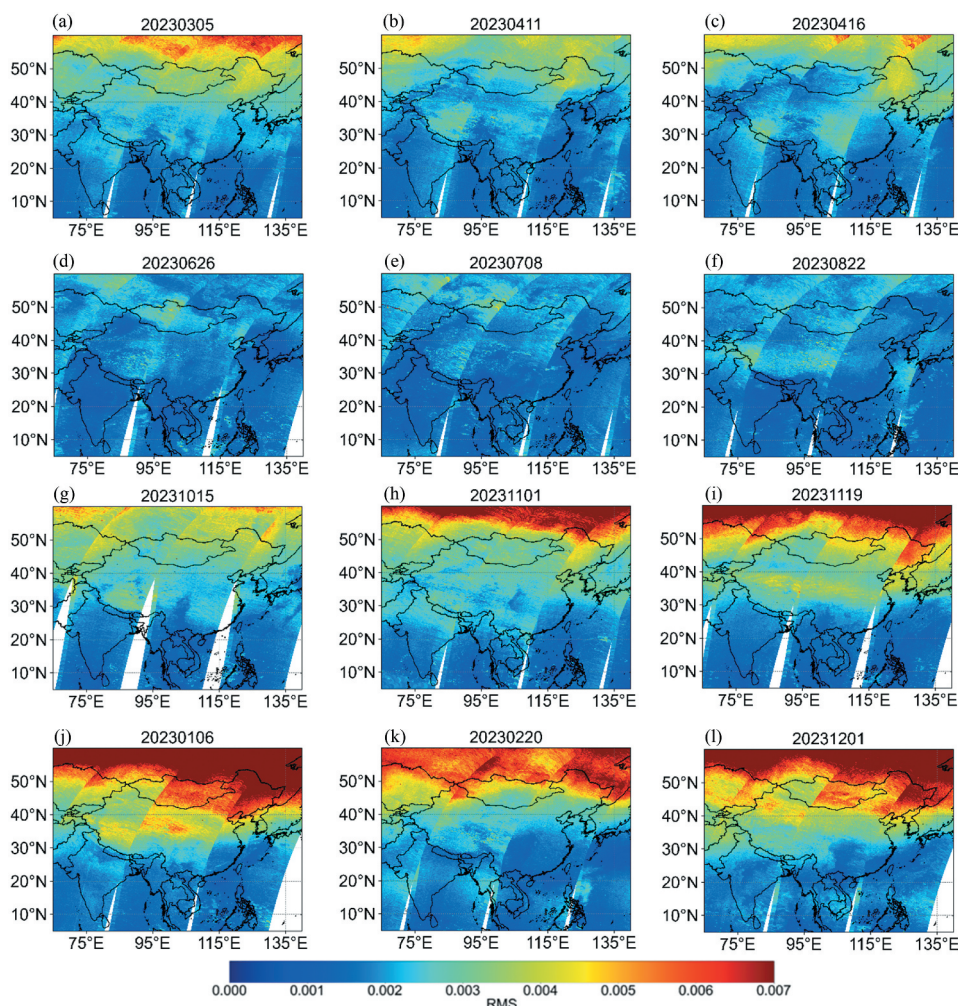
This study assessed the performance of SO<sub>2</sub> retrievals from EMI-II over China in 2023, using the RMS of spectral fitting residuals as a quality indicator. A smaller RMS in the DOAS algorithm indicated a closer match between the fitted and actual absorption spectra. Conversely, a high RMS often implied potential issues such as instrumental errors, poor data quality, or retrieval failure (Javed et al. 2021). Given China's extensive latitudinal span (approximately between 18°N and 54°N), SZA varied considerably across the country, influencing ultraviolet absorption and atmospheric scattering. These variations in observation geometry and atmospheric conditions directly impacted the quality of SO<sub>2</sub> retrievals from satellite instruments such as EMI-II.

Figure 5 illustrated the spatial distribution of RMS values across selected dates representing the seasons of 2023 over China. The results demonstrated pronounced spatio-temporal patterns in the performance of EMI-II SO<sub>2</sub> retrievals. Spatially, RMS values were typically higher at the edges of each satellite scene and in high-latitude regions. Temporally, a clear seasonal trend was observed, with the highest RMS values occurring in winter, followed by autumn and spring, while summer consistently showed the lowest values. In the study area, the RMS values of EMI-II retrievals generally ranged from  $9 \times 10^{-4}$  to  $4 \times 10^{-3}$  in summer and from  $2 \times 10^{-3}$  to  $1 \times 10^{-2}$  in winter.

Such spatiotemporal variations were likely driven by three main contributing factors: (1) larger viewing angles at the scene edges increased pixel size and reduced spatial resolution, leading to lower retrieval accuracy compared to central pixels (Deneke et al. 2021); (2) larger SZA in high-latitude regions reduced SNR, and combined with strong O<sub>3</sub> absorption, further degraded SO<sub>2</sub> retrievals (Nowlan et al. 2011); and (3) seasonal increases in SZA during winter caused significant SNR reductions, making it particularly challenging for EMI-II to accurately detect SO<sub>2</sub> signals in northern high-latitude regions (Qu et al. 2019).

The spatial distribution of RMS values reflected the retrieval quality and indicated the sensitivity of SO<sub>2</sub> detection to regional and seasonal factors. In high-latitude regions,





**Figure 5.** Seasonal comparison of RMS values for EMI-II SO<sub>2</sub> retrievals over China: (a–c) spring, (d–f) summer, (g–i) autumn, and (j–l) winter distributions.

especially in northern China during winter, large SZA persisted, and SNR was low. The EMI-II instrument frequently failed to detect valid SO<sub>2</sub> signals in these areas, even when anthropogenic emissions were likely present. Under these conditions, elevated RMS values suggested degraded spectral fitting, and even caused retrieval failures. These findings underscored the limitations of ultraviolet-based SO<sub>2</sub> retrievals under high-SZA conditions. These challenges are not unique to EMI-II; at high latitudes, TROPOMI and OMPS likewise experience degraded sensitivity and increased uncertainties under large SZA conditions (V. Fioletov et al. 2020; Li et al. 2024).

### 3.3. Sensitivity analysis and detection limits

To assess the factors influencing the accuracy of SO<sub>2</sub> retrievals, we conducted radiative transfer simulations using the SCIATRAN model. These simulations quantified the

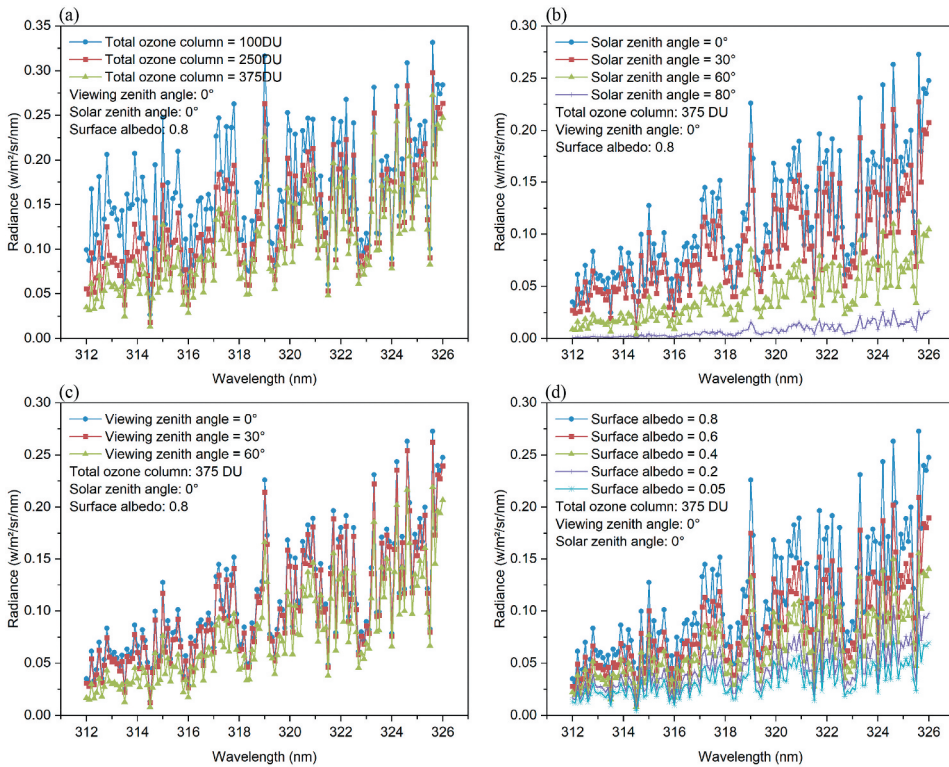


**Figure 6.** Radiance within the wavelength range of 312–326 nm as a function of (a) TOC, (b) SZA, (c) VZA, and (d) surface albedo.

influence of TOC, SZA, VZA, and surface albedo on the measured radiance and, consequently, on the accuracy of  $\text{SO}_2$  retrievals by EMI-II.

The simulation results (Figure 6) demonstrated how these parameters impacted radiance within the 312–326 nm spectral range. Specifically, when other parameters were kept constant, the radiance exhibited a decreasing trend with increasing TOC, SZA, and VZA, whereas it showed an increasing trend with increasing surface albedo.

The strong ozone absorption in the 312–326 nm range significantly weakened the  $\text{SO}_2$  absorption signal, making detection more challenging, particularly in high-latitude regions with elevated ozone concentrations. Increased SZA further lengthened the atmospheric path, enhanced absorption and scattering, decreased top-of-atmosphere radiance, and lowered the SNR. These effects were especially pronounced in winter at high latitudes, with high ozone levels and SZA, resulting in greater retrieval uncertainty. Similarly, increasing VZA reduced radiance due to a longer atmospheric path and enhanced scattering, further weakening the  $\text{SO}_2$  signal. At the edges of the satellite swath,  $\text{SO}_2$  absorption features became more diffuse and weaker, making retrievals more susceptible to noise and thus reducing accuracy. Notably, high surface albedo introduced retrieval biases due to enhanced surface reflection and non-Lambertian effects (Lorente et al. 2018). These radiative variations directly affected the strength and clarity of  $\text{SO}_2$  absorption signals, thereby influencing retrieval accuracy.

To comprehensively evaluate the performance of the EMI-II instrument in measuring  $\text{SO}_2$  concentrations, we estimated the instrument's detection limit for  $\text{SO}_2$  SCD. Under ideal measurement conditions, the detection limit for  $\text{SO}_2$  SCD was approximated by the ratio of the RMS of the spectral fitting residuals to the peak-to-peak optical density of  $\text{SO}_2$  within the fitting window (Schönhardt et al. 2008). The RMS values for  $\text{SO}_2$  retrievals typically ranged from  $1 \times 10^{-3}$  to  $4 \times 10^{-3}$ . Based on these values, the minimum detectable  $\text{SO}_2$  SCD by the EMI-II instrument was estimated to range from approximately 0.15 to 0.5 DU. Consequently,  $\text{SO}_2$  column densities below this threshold might have been overestimated due to their proximity to the instrument's detection limit.

## 4. Conclusions

This study utilized Gaofen-5 EMI-II UV2 band observation data and the DOAS algorithm to retrieve  $\text{SO}_2$  VCD from natural volcanic and anthropogenic emissions. The retrieval results were compared with those from TROPOMI and OMPS to evaluate EMI-II monitoring capabilities. By analysing the spatial distribution of  $\text{SO}_2$  concentrations, this study assessed EMI-II's performance under different emission scenarios, highlighting its potential for global atmospheric  $\text{SO}_2$  monitoring.

For natural volcanic pollution, such as the Tonga eruption, EMI-II successfully captured the westward migration of the  $\text{SO}_2$  plumes in agreement with TROPOMI observations. For anthropogenic pollution, high-emission regions such as eastern India served as representative examples. EMI-II demonstrated strong consistency with TROPOMI and OMPS, effectively capturing substantial  $\text{SO}_2$  pollution associated with major coal-fired power plants in eastern India, a region characterized by intense anthropogenic emissions. In heavily polluted areas ( $17^\circ\text{--}25^\circ\text{N}$ ,  $76^\circ\text{--}88^\circ\text{E}$ ), the spatial correlation coefficients between EMI-II and TROPOMI, and between EMI-II and OMPS, were 0.71 and 0.62, respectively. These results underscored the capability of EMI-II to monitor high  $\text{SO}_2$  emissions in industrial regions with considerable anthropogenic activity.

However, EMI-II exhibited certain limitations in high-latitude regions of northern China, where larger SZA, lower SNR, and strong ozone absorption constrained its retrieval performance. Sensitivity analysis using the SCIATRAN model indicated that variations in TOC, SZA, VZA, and surface albedo significantly affected the observed radiance, impacting the accuracy of  $\text{SO}_2$  retrievals. EMI-II showed retrieval RMS values ranging from  $1 \times 10^{-3}$  to  $4 \times 10^{-3}$ , corresponding to a detection limit for  $\text{SO}_2$  SCD of approximately 0.15 and 0.5 DU, below which concentrations might have been overestimated due to limited instrument sensitivity.

Future work will address key factors influencing EMI-II retrieval performance, including spectral calibration errors, radiometric calibration issues at the CCD edge field of view, and ozone absorption effects identified in the sensitivity analysis. These improvements will further solidify EMI-II's role in supporting regional pollution source analysis, environmental management, and global atmospheric research.

## Disclosure statement

No potential conflict of interest was reported by the author(s).



## Funding

This work was supported by The Major Project of High Resolution Earth Observation System [30-Y60B01-9003-22/23].

## ORCID

Keke Zhu  <http://orcid.org/0009-0002-3057-2133>

Yihui Huang  <http://orcid.org/0009-0001-3466-0192>

## Data availability statement

The data that support the findings of this study are available from the corresponding author upon reasonable request.

## References

- Carn, S. A., K. Yang, A. J. Prata, and N. A. Krotkov. 2015. "Extending the Long-Term Record of Volcanic SO<sub>2</sub> Emissions with the Ozone Mapping and Profiler Suite Nadir Mapper." *Geophysical Research Letters* 42 (3): 925–932. <https://doi.org/10.1002/2014gl062437>.
- Chance, K., and R. L. Kurucz. 2010. "An Improved High-Resolution Solar Reference Spectrum for earth's Atmosphere Measurements in the Ultraviolet, Visible, and Near Infrared." *Journal of Quantitative Spectroscopy & Radiative Transfer* 111 (9): 1289–1295. <https://doi.org/10.1016/j.jqsrt.2010.01.036>.
- Chance, K. V., and R. J. D. Spurr. 1997. "Ring Effect Studies: Rayleigh Scattering, Including Molecular Parameters for Rotational Raman Scattering, and the Fraunhofer Spectrum." *Applied Optics* 36 (21): 5224. <https://doi.org/10.1364/ao.36.005224>.
- Deneke, H., C. Barrientos-Velasco, S. Bley, A. Hünnerbein, S. Lenk, A. Macke, J. Fokke Meirink, et al. 2021. "Increasing the Spatial Resolution of Cloud Property Retrievals from Meteosat SEVIRI by Use of Its High-Resolution Visible Channel: Implementation and Examples." *Atmospheric Measurement Techniques* 14 (7): 5107–5126. <https://doi.org/10.5194/amt-14-5107-2021>.
- Fioletov, V. E., C. A. McLinden, N. Krotkov, C. Li, J. Joiner, N. Theys, S. Carn, and M. D. Moran. 2016. "A Global Catalogue of Large SO<sub>2</sub> Sources and Emissions Derived from the Ozone Monitoring Instrument." *Atmospheric Chemistry & Physics* 16 (18): 11497–11519. <https://doi.org/10.5194/acp-16-11497-2016>.
- Fioletov, V., C. A. McLinden, D. Griffin, N. Theys, D. G. Loyola, P. Hedelt, N. A. Krotkov, and C. Li. 2020. "Anthropogenic and Volcanic Point Source SO<sub>2</sub> Emissions Derived from TROPOMI on Board Sentinel-5 Precursor: First Results." *Atmospheric Chemistry & Physics* 20 (9): 5591–5607. <https://doi.org/10.5194/acp-20-5591-2020>.
- Fleischmann, O. C., M. Hartmann, J. P. Burrows, and J. Orphal. 2004. "New Ultraviolet Absorption Cross-Sections of bro at Atmospheric Temperatures Measured by Time-Windowing Fourier Transform Spectroscopy." *Journal of Photochemistry and Photobiology A, Chemistry* 168 (1–2): 117–132. <https://doi.org/10.1016/j.jphotochem.2004.03.026>.
- Garg, A., P. R. Shukla, S. Bhattacharya, and V. K. Dadhwal. 2001. "Sub-Region (District) and Sector Level SO<sub>2</sub> and NO<sub>x</sub> Emissions for India: Assessment of Inventories and Mitigation Flexibility." *Atmospheric Environment* 35 (4): 703–713. [https://doi.org/10.1016/s1352-2310\(00\)00316-2](https://doi.org/10.1016/s1352-2310(00)00316-2).
- Javed, Z., T. Aimon, M. Bilal, W. Su, C. Xia, A. Rehman, Y. Zhang, et al. 2021. "Recommendations for HCHO and SO<sub>2</sub> Retrieval Settings from MAX-DOAS Observations Under Different Meteorological Conditions." *Remote Sensing* 13 (12): 2244–2244. <https://doi.org/10.3390/rs13122244>.
- Kajino, M., H. Ueda, K. Sato, and T. Sakurai. 2011. "Spatial Distribution of the Source-Receptor Relationship of Sulfur in Northeast Asia." *Atmospheric Chemistry & Physics* 11 (13): 6475–6491. <https://doi.org/10.5194/acp-11-6475-2011>.

- Kong, L., X. Tang, Z. Wang, J. Zhu, J. Li, H. Wu, Q. Wu, et al. 2024. "Changes in Air Pollutant Emissions in China During Two Clean-Air Action Periods Derived from the Newly Developed Inversed Emission Inventory for Chinese Air Quality (CAQIEI)." *Earth System Science Data* 16 (9): 4351–4387. <https://doi.org/10.5194/essd-16-4351-2024>.
- Krotkov, N. A., C. A. McLinden, C. Li, L. N. Lamsal, E. A. Celarier, S. V. Marchenko, W. H. Swartz, et al. 2016. "Aura OMI Observations of Regional SO<sub>2</sub> and NO<sub>2</sub> Pollution Changes From 2005 to 2015." *Atmospheric Chemistry & Physics* 16 (7): 4605–4629. <https://doi.org/10.5194/acp-16-4605-2016>.
- Lee, C., A. Richter, M. Weber, and J. P. Burrows. 2008. "SO<sub>2</sub> Retrieval from SCIAMACHY Using the Weighting Function DOAS (WFDOS) Technique: Comparison with Standard DOAS Retrieval." *Atmospheric Chemistry & Physics* 8 (20): 6137–6145. <https://doi.org/10.5194/acp-8-6137-2008>.
- Li, C., N. A. Krotkov, S. Carn, Y. Zhang, R. J. D. Spurr, and J. Joiner. 2017. "New-Generation NASA Aura Ozone Monitoring Instrument (OMI) Volcanic SO<sub>2</sub> Dataset: Algorithm Description, Initial Results, and Continuation with the Suomi-NPP Ozone Mapping and Profiler Suite (OMPS)." *Atmospheric Measurement Techniques* 10 (2): 445–458. <https://doi.org/10.5194/amt-10-445-2017>.
- Li, C., N. A. Krotkov, J. Joiner, F. Vitali, C. McLinden, D. Griffin, S. Carn, C. Seftor, and A. Vasilkov. 2024. "Version 1 NOAA-20/OMPS Nadir Mapper Total Column SO<sub>2</sub> Product: Continuation of NASA Long-Term Global Data Record." *Earth System Science Data* 16 (9): 4291–4309. <https://doi.org/10.5194/essd-16-4291-2024>.
- Li, C., C. McLinden, V. Fioletov, N. Krotkov, S. Carn, J. Joiner, D. Streets, et al. 2018. "Author Correction: India Is Overtaking China as the World's Largest Emitter of Anthropogenic Sulfur Dioxide." *Scientific Reports* 8 (1). <https://doi.org/10.1038/s41598-018-26657-1>.
- Lorente, A., K. Folkert Boersma, L. G. T. Stammes Piet, A. Richter, H. Yu, K. Said, and J.-P. Muller. 2018. "The Importance of Surface Reflectance Anisotropy for Cloud and NO<sub>2</sub> Retrievals from GOME-2 and OMI." *Atmospheric Measurement Techniques* 11 (7): 4509–4529. <https://doi.org/10.5194/amt-11-4509-2018>.
- Martin, R. V. 2002. "An Improved Retrieval of Tropospheric Nitrogen Dioxide from GOME." *Journal of Geophysical Research* 107 (D20). <https://doi.org/10.1029/2001jd001027>.
- McCormick, B., C. Popp, B. Andrews, and E. Cottrell. 2015. "Ten Years of Satellite Observations Reveal Highly Variable Sulphur Dioxide Emissions at Anatahan Volcano, Mariana Islands." *Journal of Geophysical Research Atmospheres* 120 (14): 7258–7282. <https://doi.org/10.1002/2014jd022856>.
- Meller, R., and G. K. Moortgat. 2000. "Temperature Dependence of the Absorption Cross Sections of Formaldehyde Between 223 and 323 K in the Wavelength Range 225–375 nm." *Journal of Geophysical Research Atmospheres* 105 (D6): 7089–7101. <https://doi.org/10.1029/1999jd901074>.
- Niu, S., Y. Chen, R. Zhang, and Y. Feng. 2023. "How Does the Air Pollution Prevention and Control Action Plan Affect Sulfur Dioxide Intensity in China?" *Frontiers in Public Health* 11 (1119710). <https://doi.org/10.3389/fpubh.2023.1119710>.
- Nowlan, C. R., X. Liu, K. Chance, Z. Cai, T. P. Kurosu, C. Lee, and R. V. Martin. 2011. "Retrievals of Sulfur Dioxide from the Global Ozone Monitoring Experiment 2 (GOME-2) Using an Optimal Estimation Approach: Algorithm and Initial Validation." *Journal of Geophysical Research* 116 (D18). <https://doi.org/10.1029/2011jd015808>.
- Palmer, P. I., D. J. Jacob, R. M. M. Kelly Chance, R. Spurr, T. P. Kurosu, I. Bey, R. M. Yantosca, A. Fiore, and Q. Li. 2001. "Air Mass Factor Formulation for Spectroscopic Measurements from Satellites: Application to Formaldehyde Retrievals from the Global Ozone Monitoring Experiment." *Journal of Geophysical Research* 106 (D13): 14539–14550. <https://doi.org/10.1029/2000jd900772>.
- Pukite, J., S. Kühl, T. Deutschmann, U. Platt, and T. Wagner. 2010. "Extending Differential Optical Absorption Spectroscopy for Limb Measurements in the UV." *Atmospheric Measurement Techniques* 3 (3): 631–653. <https://doi.org/10.5194/amt-3-631-2010>.
- Qu, Z., D. K. Henze, C. Li, N. Theys, Y. Wang, J. Wang, W. Wang, et al. 2019. "SO<sub>2</sub> Emission Estimates Using OMI SO<sub>2</sub> Retrievals for 2005–2017." *Journal of Geophysical Research Atmospheres* 124 (14): 8336–8359. <https://doi.org/10.1029/2019jd030243>.
- Rozanov, V. V., T. Dinter, A. V. Rozanov, A. Wolanin, A. Bracher, and J. P. Burrows. 2017. "Radiative Transfer Modeling through Terrestrial Atmosphere and Ocean Accounting for Inelastic Processes: Software Package SCIATRAN." *Journal of Quantitative Spectroscopy & Radiative Transfer* 194: 65–85. <https://doi.org/10.1016/j.jqsrt.2017.03.009>.

- Schönhardt, A., A. Richter, F. Wittrock, H. G. Kirk, H. Oetjen, K. R. Howard, and P. B. John. 2008. "Observations of Iodine Monoxide Columns from Satellite." *Atmospheric Chemistry & Physics* 8 (3): 637–653. <https://doi.org/10.5194/acp-8-637-2008>.
- Serdyuchenko, A., V. Gorshchev, M. Weber, W. Chehade, and J. P. Burrows. 2014. "High Spectral Resolution Ozone Absorption Cross-Sections – Part 2: Temperature Dependence." *Atmospheric Measurement Techniques* 7 (2): 625–636. <https://doi.org/10.5194/amt-7-625-2014>.
- Theys, N., I. De Smedt, J. van Gent, T. Danckaert, T. Wang, F. Hendrick, T. Stavrakou, et al. 2015. "Sulfur Dioxide Vertical Column DOAS Retrievals from the Ozone Monitoring Instrument: Global Observations and Comparison to Ground-Based and Satellite Data." *Journal of Geophysical Research Atmospheres* 120 (6): 2470–2491. <https://doi.org/10.1002/2014jd022657>.
- Theys, N., P. Hedelt, I. De Smedt, C. Lerot, H. Yu, J. Vlietinck, M. Pedernana, et al. 2019. "Global Monitoring of Volcanic SO<sub>2</sub> Degassing with Unprecedented Resolution from TROPOMI Onboard Sentinel-5 Precursor." *Scientific Reports* 9 (1). <https://doi.org/10.1038/s41598-019-39279-y>.
- Theys, N., F. Vitali, C. Li, S. Isabelle De, L. Christophe, C. A. McLinden, N. A. Krotkov, et al. 2021. "A Sulfur Dioxide Covariance-Based Retrieval Algorithm (COBRA): Application to TROPOMI Reveals New Emission Sources." *Atmospheric Chemistry & Physics* 21 (22): 16727–16744. <https://doi.org/10.5194/acp-21-16727-2021>.
- Tilstra, L. G., O. N. E. Tuinder, P. Wang, and P. Stammes. 2017. "Surface Reflectivity Climatologies from UV to NIR Determined from Earth Observations by GOME-2 and SCIAMACHY." *Journal of Geophysical Research Atmospheres* 122 (7): 4084–4111. <https://doi.org/10.1002/2016jd025940>.
- Vandaele, A. C., C. Hermans, and S. Fally. 2009. "Fourier Transform Measurements of SO<sub>2</sub> Absorption Cross Sections: II.: Temperature Dependence in the 29 000–44 000 cm<sup>-1</sup> (227–345 Nm) Region." *Journal of Quantitative Spectroscopy & Radiative Transfer* 110 (18): 2115–2126. <https://doi.org/10.1016/j.jqsrt.2009.05.006>.
- Vandaele, A. C., C. Hermans, P. C. Simon, M. Carleer, R. Colin, S. Fally, M. F. Mérienne, A. Jenouvrier, and B. Coquart. 1998. "Measurements of the NO<sub>2</sub> Absorption Cross-Section from 42 000 cm<sup>-1</sup> to 10 000 cm<sup>-1</sup> (238–1000 Nm) at 220 K and 294 K." *Journal of Quantitative Spectroscopy & Radiative Transfer* 59 (3–5): 171–184. [https://doi.org/10.1016/s0022-4073\(97\)00168-4](https://doi.org/10.1016/s0022-4073(97)00168-4).
- Xia, C., C. Liu, Z. Cai, H. Wu, Q. Li, and M. Gao. 2024. "Tracking SO<sub>2</sub> Plumes from the Tonga Volcano Eruption with Multi-Satellite Observations." *IScience* 27 (4): 109446–109446. <https://doi.org/10.1016/j.isci.2024.109446>.
- Yang, K., R. R. Dickerson, S. A. Carn, C. Ge, and J. Wang. 2013. "First Observations of SO<sub>2</sub> from the Satellite Suomi NPP OMPS: Widespread Air Pollution Events Over China." *Geophysical Research Letters* 40 (18): 4957–4962. <https://doi.org/10.1002/grl.50952>.
- Yang, T., F. Si, W. Ping, Y. Luo, H. Zhou, and M. Zhao. 2020. "Research on Cloud Fraction Inversion Algorithm of Environmental Trace Gas Monitoring Instrument." *Acta Optica Sinica* 40 (9): 0901001. <https://doi.org/10.3788/aos202040.0901001>.